energies

MDPI

Article

Numerical Simulation of CO_2-EGR and Storage by Injecting Supercritical CO_2 and Water in Depleted Gas Reservoirs

Adeltus Novat Rweyemamu [1,2,*], Yuichi Sugai [1], Takehiro Esaki [1] and Theodora Tambaria [1]

[1] Laboratory of Resource Production and Safety, Department of Earth Resources Engineering, Graduate School of Engineering, Kyushu University, 744 Motooka, Fukuoka 819-0395, Japan; sugai@mine.kyushu-u.ac.jp (Y.S.); esaki@mine.kyushu-u.ac.jp (T.E.); tambaria.noely.theodora.921@m.kyushu-u.ac.jp (T.T.)

[2] Department of Petroleum Science and Engineering, School of Mines and Geosciences, University of Dar es Salaam, Dar es Salaam P.O. Box 35052, Tanzania

* Correspondence: rweyemamu.adeltus.104@s.kyushu-u.ac.jp

Abstract

The injection of CO_2 into mature natural gas reservoirs is widely recognised for its potential to store carbon dioxide while simultaneously enhancing natural gas recovery. However, across all reservoir pressure and temperature ranges, CO_2 and natural gas are miscible, leading to contamination of the produced gas and increasing surface processing costs. Although miscibility has been a limiting factor in deploying CO_2-EGR-based projects, several strategies have been proposed to mitigate it. In this study, we have analysed the inclusion of water in the CO_2 injection process to reduce mixing, improve natural displacement, and improve carbon dioxide storage security through solubility and residual trapping mechanisms. The simulation was conducted in a 3D reservoir using the CMG-GEM simulator. The results show that the inclusion of water injection improves natural gas recovery by up to 8.04% compared with when only CO_2 was injected. The CO_2 breakthrough time increased by up to 931 days, while the hysteresis and solubility trapped CO_2 were improved by 2.68% and 3.06%, respectively. EGR and CO_2 storage security were found to be affected by reservoir heterogeneity, injection rate, and the perforation depths of injector and producer wells.

Keywords: enhanced gas recovery; CO_2 storage; CO_2 injection; water injection; numerical reservoir simulation

Academic Editor: Reza Rezaee

Received: 29 May 2026
Revised: 2 July 2026
Accepted: 9 July 2026
Published: 14 July 2026

1. Introduction

Natural gas is regarded as a fuel for the energy transition as clean and renewable energies continue to mature both technologically and economically. For this reason, natural gas demand has increased due to the major policy push towards its utilisation [1]. Different engineering approaches, including developing new fields and improving recovery from mature reservoirs through compression and fluid injection, are being applied to increase natural gas production to meet the demand. However, natural gas by itself remains a source of emissions as a fossil fuel, and thus, in the long term, it may not mitigate climate change concerns [2,3] and is therefore not a good solution towards reducing global warming below 2 °C, as required by international climate agreements [4]. Carbon Capture Utilisation and Storage with Enhanced Gas Recovery (CCUS-EGR) is becoming a strategic industry in the transition to net-zero emissions from gas fuels by increasing natural gas

production without emitting carbon dioxide into the atmosphere [5–7]. It involves injecting CO_2 captured from large emitting point sources into a mature gas reservoir. This process promotes natural gas recovery by displacing and repressurising the reservoir while permanently sequestering carbon dioxide [8,9].

The use of CO_2 to enhance gas recovery has been widely studied for its technical and economic feasibility. Early research on CO_2-EGR by Van Der Burgt et al. [10] indicated an increase in natural gas recovery when CO_2 was injected into a producing gas reservoir. Oldenburg et al. [11,12] reported additional methane production during and after injection. This improvement in gas recovery is attributed to the density difference between carbon dioxide and methane and to reservoir repressurisation as injected CO_2 advances through the pores by advection and diffusion, pushing methane ahead of it under the control of either interstitial velocity or concentration gradient [9].

During diffusion-driven displacement, injected CO_2 contaminates the natural gas, forming a mixing zone that is critical to displacement efficiency. Miscibility arises from the absence of an interface between natural gas and carbon dioxide, and therefore, the entire EGR process is driven by pore pressure maintenance and miscible displacement (CO_2 miscibly displacing natural gas) [13]. However, Amin et al. [14] reported the presence of IFT between supercritical CO_2 and CH_4, based on experimental results obtained using the pendant drop method in the temperature range of 368.15–433.15 K and pressures between 6.9 and 41.37 MPa. Although thermodynamically a stable interface exists only between two immiscible fluids, the experimental results indicated IFT values ranging from 0.00036 to 0.01211 dyne/cm for the CH_4-CO_2 interface.

The rate at which injected carbon dioxide contaminates natural gas assets in the reservoir remains a major drawback of CO_2-EGR. The magnitude of contamination can be minimised by optimising reservoir management, injection, and production measures. Injection rate and timing, distance between the injector and producer well, reservoir heterogeneity, connate water saturation, connate salinity, and well perforation depth are among the factors that affect miscibility [15–17]. Injection of carbon dioxide to enhance gas production requires the reservoir to be somewhat depleted to prevent injection pressure from exceeding the initial reservoir pressure prematurely. Injection of CO_2 after conventional depletion of the gas reservoir improves gas recovery compared with early injection [18]. A higher injection rate leads to a higher methane production rate and a shorter injection cycle, resulting in a reduced net recovery factor. A lower injection rate leads to a lower production rate, longer production time, and reduced CO_2 diffusion, resulting in CO_2 migrating as a plume rather than an irregularly diffused phase [19]. Injection of CO_2 at the lower portion of the reservoir, with the production well perforated in the top stratum, repressurises the reservoir, efficiently improves sweep of natural gas from the bottom layers towards the production well, and minimises contamination and gas mixing in the upper part of the reservoir [15]. In heterogeneous reservoirs, a higher-permeability zone becomes a preferential flow path for CO_2 towards the production well, thereby affecting the efficiency of natural gas displacement and causing early breakthrough [20,21]. Higher CO_2 dispersivity and reduced displacement efficiency were observed in a heterogeneous reservoir than in a homogeneous one [22]. The effect of connate water in CCUS-EGR is not entirely consistent. Patel et al. [23] report that connate water delays CO_2 breakthrough while simultaneously reducing CH_4 production, whereas He et al. [24] observe the opposite behaviour, while Zecca et al. [25] concluded that CO_2 dispersivity increases with connate water saturation. Nevertheless, both lines of work reach a shared conclusion: under significant connate water saturation, net CO_2 storage is reduced, and the fraction of CO_2 stored via residual and solubility trapping increases. Abba et al. [17] concluded lower dispersion of CO_2 into CH_4 in a reservoir with higher connate salinity.

Miscibility, natural gas contamination, and early CO_2 breakthrough remain the main drawbacks of CCUS-EGR, but several studies have focused on reducing CO_2 mobility to address these issues. The injection of carbonated water, followed by CO_2 injection, increased the recovery factor, CO_2 storage, and delayed breakthrough in a heterogeneous reservoir with higher permeability at the bottom of the formation [26]. The injection of a gelling fluid to limit carbon dioxide mobility, delay breakthrough, and improve sweep showed minimal impact on breakthrough [16].

Since the presence of connate water has been shown to delay CO_2 breakthrough and improve storage security, in this study we suggest including water in the CO_2 injection process to reduce CO_2 mobility, reduce miscibility, and improve storage security. In gas reservoirs, water injection is reported to be an effective method for EGR, especially in a volumetric-drive reservoir near abandonment pressure [27]. Although a favourable mobility ratio, volumetric sweep, displacement efficiency, and unaltered natural gas composition are among the advantages of water injection, in most effective water-EGR projects, water injection is considered as a method for pressure maintenance by filling the voidage space created as a result of depletion and keeping the reservoir pressure above dew point pressure [28,29]. At higher reservoir abandonment pressure, water injection for EGR requires a higher injection rate, resulting in natural gas entrapment and water breakthrough in the production well, leading to liquid loading [30]. For a feasible water-EGR project, the drawback may still be the high volume of water required relative to the volume of gas due to compressibility difference [31,32].

Unlike the previous study by He et al. [24] in a subcritical reservoir and Patel et al. [23] in a supercritical reservoir, where connate/irreducible water was included in the simulation of CO_2-EGR as an immobile phase, and the study by Omari et al. [26], where water with already dissolved CO_2 was initially injected in a subcritical reservoir for pressure build-up before supercritical CO_2 injection, this study proposes to inject CO_2 and water in a depleted gas reservoir at pressures above the supercritical threshold to reduce CO_2 mobility, reduce CO_2-CH_4 miscibility, improve sweep and displacement efficiency, and increase CO_2 storage security through solubility and hysteresis trapping. To illustrate the potential of the water–CO_2 EGR strategy, the effects of different reservoir and injection parameters, such as heterogeneity, injected water–CO_2 fractions, injector/producer well depth, and strategy, are investigated using a numerical reservoir simulator and discussed in terms of natural gas recovery and CO_2 storage.

2. Theory

In the CO_2-EGR system, fluid flow is primarily driven by the pressure gradient between the injector and producer wells. The general forms of equations governing the fluid flow and mixing include the mass and energy conservation equations, Darcy's law, and the fluid and rock constitutive relations. In multicomponent–multiphase flow, the equations are applied for each component [20,21,23]. Assuming the reservoir rock is rigid and chemically inert to the injected fluid throughout the simulation time, and that the temperature remains constant, the equation reduces to Darcy's equation. The mass conservation equation for any component in a multiphase system is given by Equation (1).

$$\frac{\partial}{\partial t}\left(\phi \sum_{\beta} \rho_\beta S_\beta X_\beta^\kappa\right) + \nabla . F^\kappa + \nabla . \mathcal{U}^\kappa = q^\kappa \quad (1)$$

where ϕ is the porosity of the media, ρ_β and S_β represent density and saturation of phase β respectively, X_β^κ is the mass fraction of component κ in phase β, F^κ is the net mass flux, $\mathcal{U}^\kappa$ is the molecular diffusion rate, and q^κ is the source/sink mass rate. The mass flux F^κ in Darcy's form is given by Equation (2), while the molecular diffusion $\mathcal{U}^\kappa$

of components in the gas and aqueous phases is governed by Fick's law as presented in Equation (3) [20]:

$$F^{\kappa} = \sum_{\beta} X_{\beta}^{\kappa} u_{\beta} \tag{2}$$

$$\mathcal{U}^{\kappa} = \frac{D_{\beta}^{\kappa}}{\tau_{\beta}} \phi \rho_{\beta} S_{\beta} \nabla X_{\beta}^{\kappa} \tag{3}$$

$$u_{\beta} = -k \frac{k_{r\beta} \rho_{\beta}}{\mu_{\beta}} \left(\nabla P_{\beta} - \rho_{\beta} g \right) \tag{4}$$

where D_{β}^{κ} is the diffusion coefficient of component k in phase β, and τ_{β} is the tortuosity of the rock. Equation (4) represents Darcy's velocity of each phase u_{β}, where k is the absolute permeability tensor, $k_{r\beta}$ is the phase relative permeability, μ_{β} is the viscosity of phase β, g is the gravitational acceleration, and P_{β} is the pressure of phase β given as $P_{\beta} = P + P_{c\beta}$, with P being the pressure of the reference phase and $P_{c\beta}$ as the capillary pressure. Density and viscosity of each phase are estimated from the PR-EOS present in Equation (5):

$$P = \frac{RT}{V - b} - \frac{a}{V^2 - 2Vb + b^2} \tag{5}$$

The solubility of CH_4 in water is neglected because it is much lower than that of CO_2, implying that it exists only in the gaseous phase [23,24]. Both CO_2 and water components exist in gaseous and aqueous phases. Therefore, the continuity equation for each component is presented in Equations (6)–(8):

$$\frac{\partial}{\partial t}\left(\phi \sum_{\beta} \rho_g S_g X_g^{CH_4} \right) + \nabla . \left(X_g^{CH_4} u_g \right) + \nabla . \left(\frac{D_g^{CH_4}}{\tau_g} \phi \rho_g S_g \nabla X_g^{CH_4} \right) = X_g^{CH_4} q_g \tag{6}$$

$$\frac{\partial}{\partial t}\left(\phi \sum_{\beta=l,g} \rho_{\beta} S_{\beta} X_{\beta}^{CO_2} \right) + \nabla . \left(\sum_{\beta=l,g} X_{\beta}^{CO_2} u_{\beta} \right) + \nabla . \left(\frac{D_{\beta}^{CO_2}}{\tau_{\beta}} \phi \rho_{\beta} S_{\beta} \nabla X_{\beta}^{CO_2} \right) = \sum_{\beta=l,g} X_{\beta}^{CO_2} q_{\beta} \tag{7}$$

$$\frac{\partial}{\partial t}\left(\phi \sum_{\beta=l,g} \rho_{\beta} S_{\beta} X_{\beta}^{H_2O} \right) + \nabla . \left(\sum_{\beta=l,g} X_{\beta}^{H_2O} u_{\beta} \right) = \sum_{\beta=l,g} X_{\beta}^{H_2O} q_{\beta} \tag{8}$$

The solubility of CO_2 in water is estimated based on the principle of fugacity, which states that at equilibrium the fugacity of the CO_2 component is equal in both phases, $f_{CO_2}^{g} = f_{CO_2}^{l}$. The fugacity of the gaseous phase is related to partial pressure, while that of the aqueous phase is calculated according to Henry's law as in Equation (9):

$$f_{CO_2}^{g} = f_{CO_2}^{l} = \varphi P_{CO_2} = H_{CO_2} x_l^{CO_2} \tag{9}$$

where $f_{CO_2}^{g}$ and $f_{CO_2}^{l}$ are fugacity of CO_2 in gaseous and aqueous phases respectively, H_{CO_2} is the Henry's constant and $x_l^{CO_2}$ is the mole fraction of CO_2 in the aqueous phase. Under different pressure conditions, Henry's constant is calculated as a function of pressure P, temperature T, universal gas constant R, and partial molar volume of CO_2 as presented in Equation (10) with the respective term defined in Equations (11) and (12):

$$InH_{CO_2} = H_{CO_2}^{sat} + \frac{1}{RT} \int_{P_{H_2O}^{sat}}^{P_M} v_{CO_2}^{\infty} dP_M \tag{10}$$

$$InH_{CO_2}^{sat} = InP_{H_2O}^{sat} - 9.4234\frac{1}{T} + 4.0087\frac{(1-T^*)^{0.355}}{T^*} + 10.3199\frac{exp(1-T^*)}{(T^*)^{0.41}} \quad (11)$$

$$v_{CO_2}^{\infty} = 37.51 - 9.585 \times 10^{-2}T_c + 8.74 \times 10^{-4}T_c^2 - 5.044 \times 10^{-7}T_c^3 \quad (12)$$

where $H_{CO_2}^{sat}$ is Henry's constant under saturation pressure conditions calculated by Harvey's method, $v_{CO_2}^{\infty}$ is the partial molar volume of CO_2 in infinitely dilute aqueous phase, and $T^* = {}^{T}/_{T_{H_2O}^c}$, where $T_{H_2O}^c$ represents the critical temperature of water and T_c is the reservoir temperature. In saline formation, Henry's constant is corrected to account for salinity using Equation (13):

$$In\left(\frac{H_{salt,CO_2}}{H_{CO_2}}\right) = K_s d_{salt} \quad (13)$$

$$K_s = 0.11572 - 6.0293 \times 10^{-4}T_c + 3.5817 \times 10^{-6}T_c^2 - 3.7772 \times 10^{-9}T_c^3 \quad (14)$$

where $H_{salt,CO2}$ is Henry's constant for CO_2 taking into account the salinity influence, d_{salt} is the molar concentration of salt in aqueous solution, and K_s is the salting-out coefficient calculated as by Equation (14).

3. Models and Methods

3.1. Model Construction and Simulation Parameters

Modelling and simulation work was conducted using the academic-licenced CMG-GEM software package version 2022.10. CMG-GEM is widely used to simulate three-dimensional multiphase and multicomponent flow in porous media. The Peng–Robinson equation of state (PR-EOS78) in the GEM module was selected to calculate phase-equilibrium compositions and fluid densities.

For validation purposes, a benchmark model used by previous researchers, Biagi et al. [33], Patel et al. [21,23], and He et al. [24], was selected to simulate 3D cases. The size of the full model is 804.76 m × 804.76 m × 45.72 m, with four producer wells at the corners and one injector well at the centre of the reservoir, making it perfectly symmetrical. A quarter of the model, with dimensions of 201.19 m × 201.19 m × 45.72 m, was used for simulation in this study as indicated in Figure 1. The simulated domain, with a thickness of 45.72 m, was divided into 44 × 44 × 10 grids, resulting in 19,260 grid blocks, each 4.572 m in size. The blocks were initially saturated with only CH_4 gas, representing natural gas at an initial reservoir pressure of 3.55 MPa and a temperature of 66.7 °C. The injector well was perforated in the reservoir's bottom layer, while the producer well was perforated in the top layer. The boundaries were assumed to be adiabatic and to have a no-flow boundary condition. To validate the model, the initial case was run using the reference model parameters. These included: a constant CO_2 injection rate of 0.1 kg/s, a constant producer well bottom hole pressure of 3.55 MPa, and a well shut-in condition of 20% CO_2 mass fraction in the produced gas stream. The final results were compared with observations from previous studies. After validation, parameters were modified to simulate supercritical CO_2-water injection as summarised in Table 1.

For the CO_2-water injection EGR, two models, referred to as Case-A and Case-B, were constructed based on the validated model: a homogeneous and a heterogeneous one, respectively as presented in Figure 2. In the Case-A model, isotropic permeability, as in the benchmark model, was assigned to all grid blocks, whereas in the Case-B model, vertical permeability variation was introduced within model layers, each with homogeneous isotropic properties. To analyse the effect of heterogeneity, three-layered reservoirs with varying Dykstra–Parsons (V_{DP}) coefficients for vertical permeability were modelled, as pre-

sented in Table 2. The average permeability and the k_h/k_v ratio were kept constant at 50 mD and 0.1, respectively. An equal porosity of 23% was assigned in all cases, resulting in a 1.5028×10^7 ft^3 reservoir pore volume. The initial mobile fluid in the reservoir for all cases was set to CH_4, occupying 85% of the pore space, with 14.999% occupied by connate water and 0.001% by nitrogen gas as a tracer element in the GEM module. The initial reservoir pressure and temperature for all cases were 19.098 MPa and 95 °C, respectively, and the boundary conditions were kept adiabatic and no-flow. The gas–water contact (GWC) was located significantly below the reservoir to eliminate the influence of the aquifer. The solubility of CO_2 in brine in the simulator was estimated using Henry's law. The relative permeability and capillary pressure were defined by the Brooks–Corey model, as given in Equations (15)–(17), where s_{wi} represents the irreducible water saturation, λ is the pore-size distribution index, P_d is the threshold pressure, and k_{rw} and k_{rg} are water and gas relative permeabilities, respectively. The hysteresis CO_2-trapping mechanism was defined using Land's model, with a maximum residual gas saturation of 40% [34,35] for relative permeability hysteresis, and the relative permeability scanning loop for each saturation change cycle was generated using a built-in linear hysteresis model. The Leverett J-function scaling approach in Equation (18) was used to assign different capillary pressure curves in each grid block according to porosity and permeability variation. Constant interfacial tension and contact angle were assumed [34,35]. The parameters used in the calculation of relative permeabilities, capillary pressure, and other reservoir parameters were as summarised in Table 1 [23]:

$$k_{rw} = \left(\frac{S_w - S_{wi}}{1 - S_{wi}}\right)^{\frac{2+3\lambda}{\lambda}} \tag{15}$$

$$k_{rg} = \left(\frac{1 - S_w}{1 - S_{wi}}\right)^2 \left[1 - \left(\frac{S_w - S_{wi}}{1 - S_{wi}}\right)^{\frac{2+\lambda}{\lambda}}\right] \tag{16}$$

$$P_c = P_d \left(\frac{S_w - S_{wi}}{1 - s_{wi}}\right)^{-\frac{1}{\lambda}} \tag{17}$$

$$J(S_w) = \frac{P_c(S_w)}{\gamma cos\theta}\sqrt{\frac{k}{\phi}} \tag{18}$$

The reservoir was initially produced by the depletion method (primary production) at a maximum constant rate of 5% PV per year until the pressure declined to approximately 8.274 MPa, which is above the supercritical pressure of CO_2, after which injection began. The fluid injection stage was simulated into two sub-stages: the EGR stage and the storage stage. In the EGR stage, the simulation was conducted to study the effect of incorporating water injection into CO_2-EGR. The total fluid injection rate was set to 5% PV per year, which served as the basis for surface water and CO_2 rate calculations. Based on the set pore volume, the injection rates ranged from 0.2005 kg/s to 0.1203 kg/s for CO_2 and from 0 kg/s to 0.2572 kg/s for water, with water fractions ranging from 0 to 0.4, respectively, as presented in Table 3. It should therefore be noted that the fluid fractions used in this study are the fractions of water in the injected pore volume.

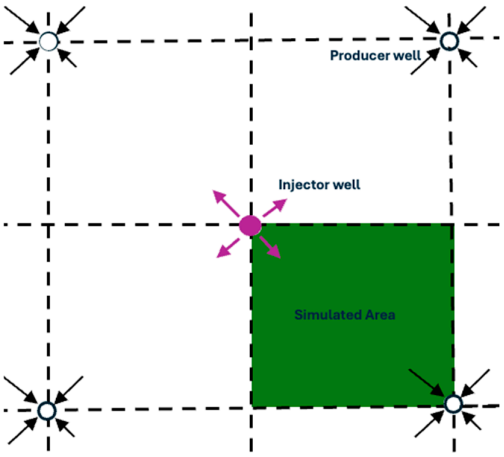

Figure 1. Five-spot injector/producer well pattern.

Table 1. Parameters used in model setup and simulation.

Property	Value
Initial reservoir pressure	19.098 MPa
Reservoir temperature	95 °C
Reservoir top	2133.6 m
Porosity	0.23
Horizontal permeability (k_h) (for homogeneous)	50 mD
Vertical permeability (k_v)	0.1 × k_h
Initial CH_4 saturation	0.85
Irreducible water saturation(S_{wi})	0.10
Pore-size distribution index (λ)	2
Threshold capillary pressure(P_d) [23]	50 kPa
Critical gas saturation (S_{gcr}) [36]	0.05
Production rate	5% PV/year
Production well bottom hole pressure	8.274 MPa
Injection CO_2-Water PV ratio	0–0.4
Total fluid injection rate	5% PV/year
CO_2 diffusion coefficient	0.006 cm^2/s
Rock compressibility	5.0 × 10^{-7}/kPa
Injector well maximum bottom hole pressure	19.098 MPa

Table 2. Permeability values used in the heterogeneous model (L1 is the bottom layer, and L10 is the top layer).

Case	V_{DP}	Source	Permeability (mD)	L1	L2	L3	L4	L5	L6	L7	L8	L9	L10
B1	0.87	Liu et al. [37]	k_h	60	60	100	5	20	90	40	5	20	100
			k_v	6	6	10	0.5	2	9	4	0.5	2	10
B2	0.49	Generated	k_h	50	30	115	35	40	110	20	25	45	30
			k_v	5	3	11.5	3.5	4	11	2	2.5	4.5	3
B3	0.29	Generated	k_h	45	60	50	35	20	65	70	30	85	40
			k_v	4.5	6	5	3.5	2	6.5	7	3	8.5	4

Table 3. Gas and water injection rates for different water fractions in the injected pore volume.

Water PV Fraction	0.0	0.02	0.05	0.10	0.15	0.20	0.25	0.30	0.35	0.40
Gas rate (kg/s)	0.2005	0.1965	0.1905	0.1804	0.1704	0.1604	0.1504	0.1403	0.1303	0.1203
Water (kg/s)	0.0000	0.0129	0.0322	0.0643	0.0965	0.1286	0.1608	0.1929	0.2251	0.2572

The production well was constrained to a maximum CO_2 mole fraction of 30% in the production well stream. A 1% CO_2 mole fraction was considered the initial carbon dioxide breakthrough, and the well was shut-in when the maximum CO_2 fraction was reached, marking the end of the EGR phase. After the production well was shut-in, operating conditions at the injection well were altered, and CO_2 injection for storage commenced. The injection well was switched to inject only CO_2, and the injection rate was increased to 5 times the initial injection rate to minimise operating time while maximising storage. Injection continued until the pressure equalled the initial reservoir pressure. When the reservoir pressure equalled the initial pressure, the injection well was shut-in, marking the end of the injection simulation. For the purpose of reservoir monitoring, the simulation was extended to a total of 100 years of simulation.

The performance of each scenario was evaluated by calculating the improved CH_4 recovery factor at the time of production well shut-in using Equation (19), the cumulative produced/recycled CO_2, the amount of CO_2 stored in the reservoir during both the EGR and storage phases, the contribution of each trapping mechanism, and the visualisation of plume migration using CMG-Results version 2022.10, Excel, and separate Python codes. The results were grouped into different cases, with Case A and Case B representing the effects of water content on EGR, CO_2 breakthrough time, and CO_2 storage for homogeneous and heterogeneous reservoirs, respectively; Case C represents the effects of perforation depth; Case D represents the effects of injection rate; and Case E shows the effect of injection strategy:

$$\mathrm{RF} = \frac{\text{Cummulative mass of } CH_4 \text{ produced}}{\text{Mass of } CH_4 \text{ in the reservoir}} \quad (19)$$

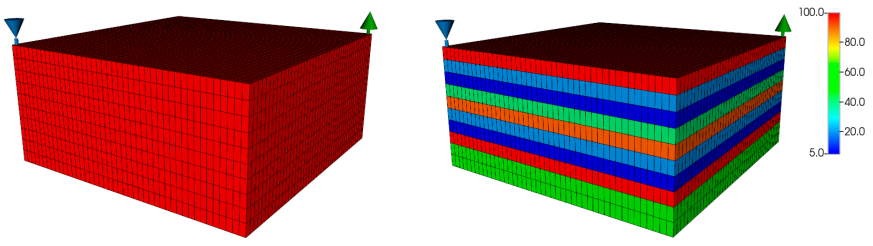

Figure 2. Simulation setup: (**a**) homogeneous model and (**b**) heterogeneous permeability model.

3.2. Model Validations

The model was validated by comparing the base-case simulated results with those from identical previous studies by He et al. [23], Biagi et al. [32], and Class et al. [34], as shown in Figure 3. The curve morphology in this study was consistent with the observations reported in the previous study. In the build-up stage of CH_4 production rate, the results of this study were slightly lower, by about 6.89%, than those of the previous study. The maximum production rate of methane was consistent with those reported by Biagi et al. and He et al. The CO_2 rate at the shut-in was consistent with observations by He et al. and Class et al. and was 22.99% lower than that of Biagi et al. Also, the results from this work indicate a 2.95% longer shut-in time (59 days) compared to Biagi et al.'s results. The CH_4 production rate at the time of shut-in for this study was higher by 3.18% and 2.21% from that of Biagi et al.'s and He et al.'s results, respectively, and was lower by 0.9% from Class et al.'s work. The observed difference could be due to other parameters, such as rock compressibility, which were not provided in some of the benchmarking models, and to the software used for simulation, which is CMG-GEM, whereas some benchmarking models used TOUGH and ECLIPSE simulators. Therefore, given the level of consistency ob-

served in the base case, the model can be confidently used to simulate other cases in this study.

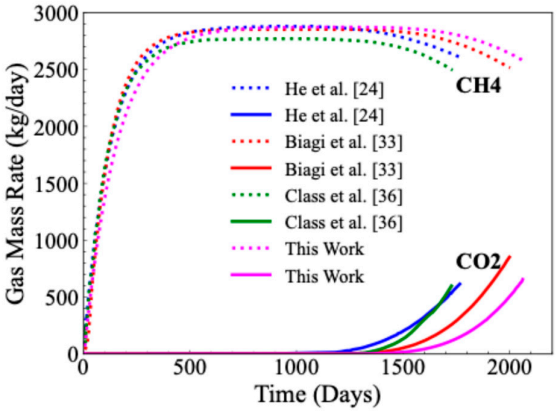

Figure 3. CO_2 and CH_4 gas mass rate comparison for different previous simulation results.

4. Results and Discussion

4.1. Effect of Water on EGR and CO_2 Storage

Figure 4a shows the effect of water on CO_2-EGR. The enhanced recovery factor values at a water fraction of 0.0 on the x-axis correspond to the case where only CO_2 was injected, while the other results reflect the effect of water content. Both Case A and Case B showed improved gas recovery upon CO_2 injection, with further gains when water was included. The use of water, together with CO_2 injection, increased recovery by an additional 1.55% in a homogeneous reservoir and up to 8.04% in a highly heterogeneous reservoir (V_{DP} = 0.87) compared with pure CO_2 injection. In both cases, gas recovery increased with increasing water content up to around 0.25 fraction, followed by a decrease in recovery. This increase in recovery upon water introduction was attributed to improved displacement efficiency, resulting from the lower mobility of the water phase in the mixture. In Case-B, the higher recovery than in Case-A could be due to water blocking the higher-permeable zone in the reservoir and forcing CO_2 to flow through the low-permeable zone, leading to higher improved recovery. All cases indicated delayed CO_2 breakthrough into the production well when water was included in the injection, whereas the breakthrough time for heterogeneous reservoirs is higher at a water fraction of 0.25, as indicated in Figure 4b.

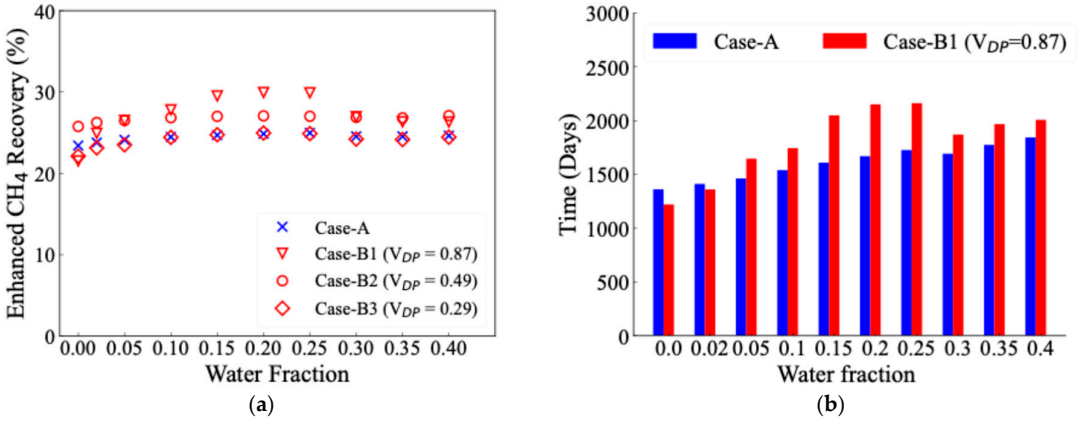

Figure 4. (**a**) Effect of water injection on gas recovery. (**b**) CO_2 breakthrough time.

Figure 5a,b represents the dynamics of the mixing zone in layer 2 of the homogeneous reservoir at the end of the first year of injection and during the time of production well shut-in, respectively, for both cases of pure CO_2 injection and when there is a 0.1 fraction. Both plots indicate a decrease in the CO_2-CH_4 mixing zone upon the introduction of water, supporting improved displacement. Figure 5b indicates that, at the time of production well shut-in, the mixing zone for pure CO_2 is 40 m, while that for CO_2 combined with water is 36 m, representing a 10% decrease in the mixing zone. The decrease in the mixing zone implies a reduction in the displacement front's inclination when water is introduced, and also improved CH_4 recovery by reducing residual CH_4 trapped therein.

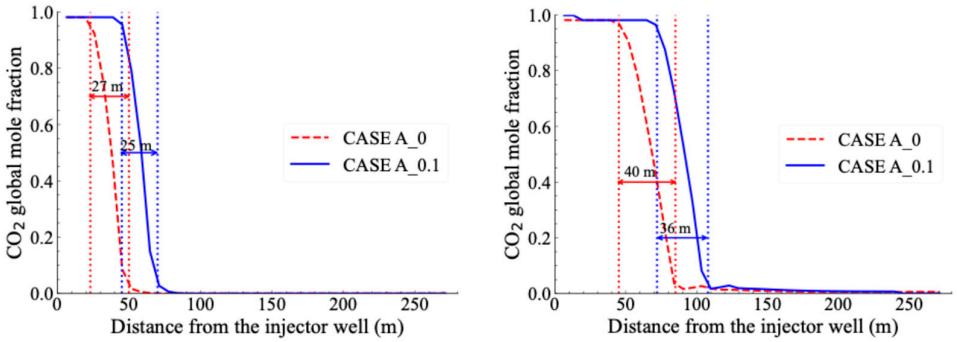

Figure 5. CO_2-CH_4 mixing zone dynamics in layer 2 during the EGR process in a homogeneous reservoir (**a**) at the end of year 1 of injection and (**b**) during well shut-in time. (Vertical dotted lines represent the size of the mixing zone, red lines represents CASE A_0, blue lines represents CASE A_0.1).

In a heterogeneous reservoir, the effect of water injection varies across layers with different permeabilities, as shown in Figure 6. In the higher-permeability zone, CO_2 migration is reduced, whereas in the lower-permeability zone, it is enhanced. This effect reduces CO_2 breakthrough by blocking higher-permeability zones and improves recovery by displacing CH_4 in lower-permeability zones. However, the CO_2-CH_4 mixing zone expands in the presence of water in both the higher- and lower-permeability zones.

Analysis of the CO_2 plume advancement in a diagonal slice from the injector to the producer well for Cases A and B1, as indicated in Figure 7a,b, respectively, shows different patterns of advancement. In Case A, the plume advances uniformly, whereas in Case B, the displacement front advances unevenly. The results also indicate an improved displacement front and a delay in CO_2 breakthrough when water is included in the injection process. As the injection continues, three distinct phases appear in both cases. This phenomenon is caused by gravity segregation, which causes water to sag in the mixture. These observations support improved recovery when water is included in the injection process.

To understand the production dynamics, the EGR simulation time was extended, and the results are presented in Figure 8. In all cases, CH_4 production increased to a peak, remained steady at the plateau rate, and then began to decline when CO_2 breakthrough occurred. The presence of water in the injection stream resulted in a lower plateau rate than when only CO_2 was injected. A slow increase in the CO_2 production rate and mole fraction in the production stream was also observed in the presence of water. The lower plateau rate can be explained by the reservoir-pressure-maintenance effect. When only CO_2 is injected into the reservoir, pressure is more easily maintained because the gas is more compressible than water. The slow increase in CO_2 mole fraction in the production stream is due to reduced CO_2 mobility.

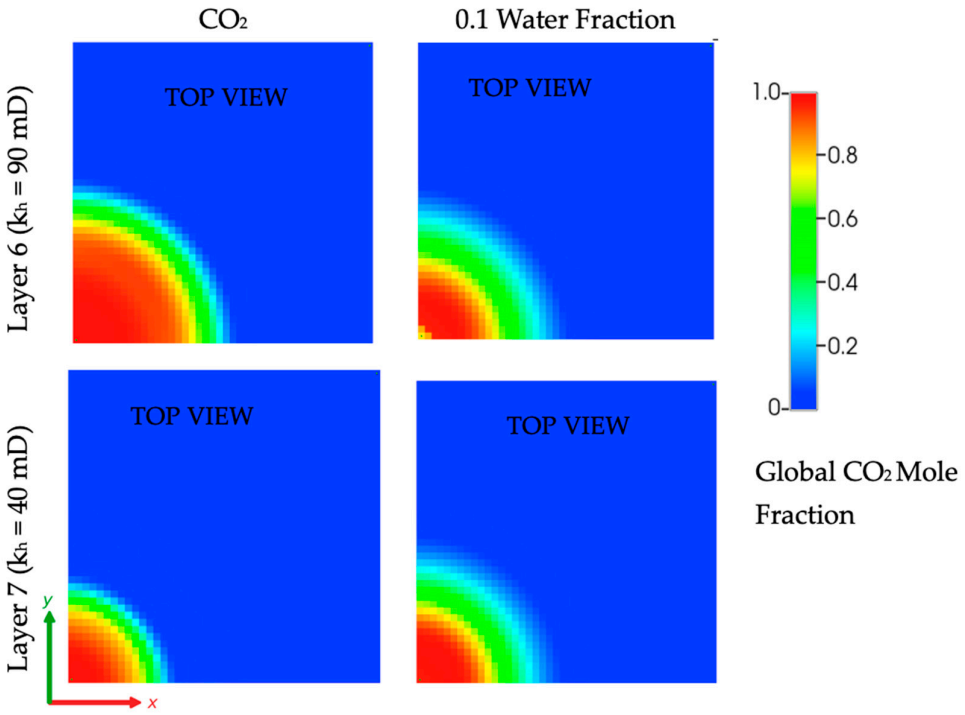

Figure 6. CO_2 global mole fraction representing the influence of water on CO_2 plume migration in higher and lower permeable layers (time = 1 year of injection).

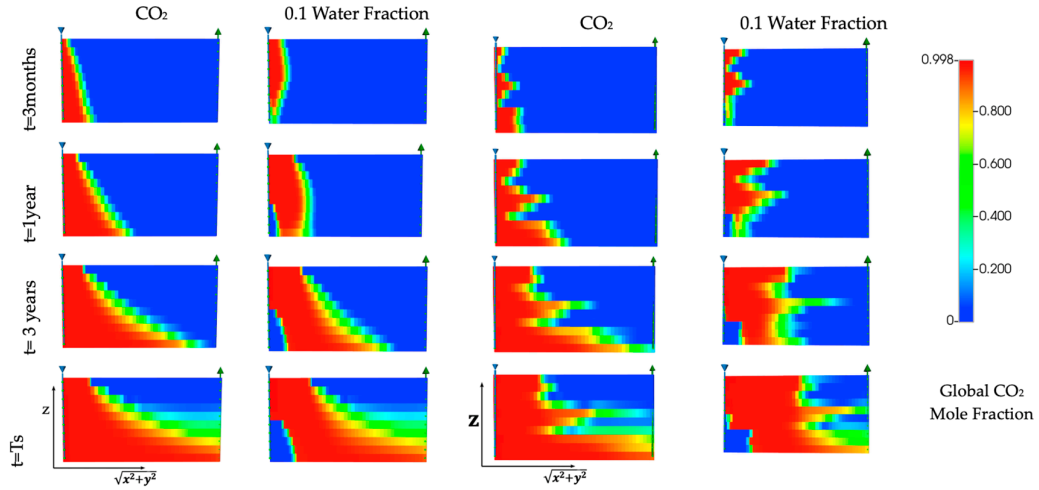

Figure 7. Global CO_2 mole fraction distribution at different times describing the effect of water on plume migration in (**a**) homogeneous and (**b**) heterogeneous reservoirs.

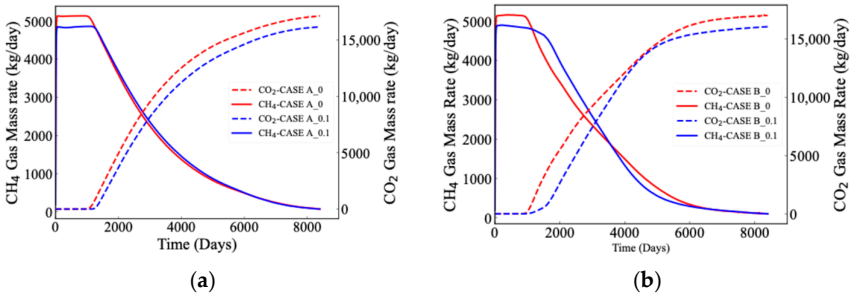

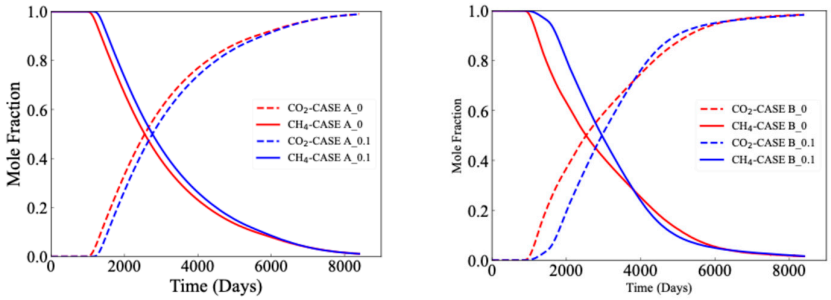

(**c**) (**d**)

Figure 8. Production well stream properties: (**a**) homogeneous reservoir gas mass rate, (**b**) heterogeneous reservoir gas mass rate, (**c**) homogeneous reservoir production mole fraction, and (**d**) heterogeneous reservoir production mole fraction.

4.2. Effect of Perforation Depth

This section analyses the effect of varying perforation depth in both producer and injector wells on CH_4 recovery and CO_2 inventory during the EGR simulation in both homogeneous and heterogeneous reservoirs. Although in CO_2-EGR cases involving only injection of CO_2, the practice has been to perforate the injector well at the bottom layers and the producer well at the top [15,24,36], in this study, the influence of perforation depth is analysed to elucidate its effect when water is in the injection stream. In all cases, the 0.1 water fraction was used.

4.2.1. Influence of Perforation Depth in a Homogeneous Reservoir

Four cases with different injector/producer well perforation placements were simulated. In case C-01, both the producer and the injector wells were fully perforated; in case C-02, a fully perforated injector well and a top-perforated producer well were used; in case C-03, the injector well was perforated in the middle of the reservoir while the producer well was perforated at the top; finally, in case C-04, the injector well was perforated in the bottom layers and the producer well was perforated at the top.

In all cases, CH_4 production gradually increased to a maximum rate, remained constant, and then declined upon CO_2 breakthrough into the production well. Case C-01 showed a rapid increase in methane production and a shorter plateau than in the other cases. As shown in Figure 9a, cases C-02, C-03, and C-04 exhibited a similar production trend during the build-up and steady-state phases but differed during the decline phase. Case C-02 showed higher recovery and a longer shut-in time. The improved recovery for Case C-02 was 29.35%, compared with 24.48%, 28.67%, and 27.46% for Cases C-01, C-03, and C-04, respectively, as shown in Figure 9b.

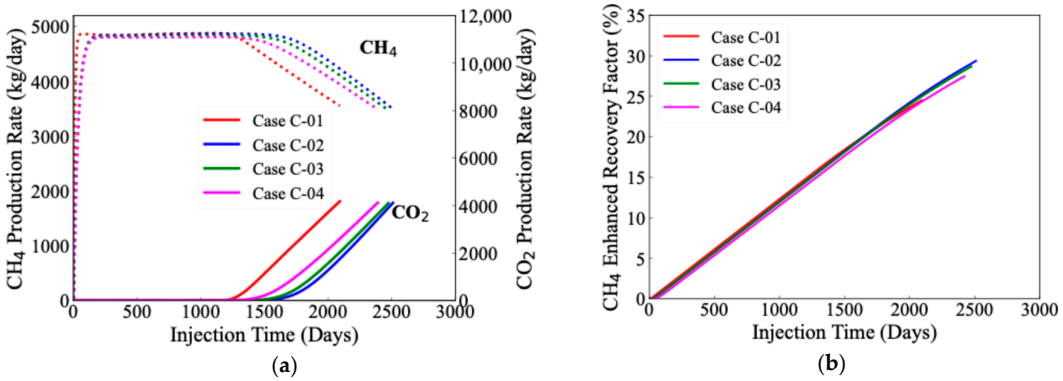

(**a**) (**b**)

Figure 9. Effect of perforation depth on EGR and CO_2 storage in homogeneous reservoir. (**a**) CH_4 and CO_2 production profile. (**b**) Enhanced CH_4 recovery.

To explain the influence of perforation depth on methane displacement, the dynamics of CO_2 mole fraction iso-surfaces in the formation, from the injector well to the producer well, were analysed. The iso-surfaces of 0.9, 0.6, and 0.1 CO_2 mole fractions, indicating regions with high, mixed, and low CO_2 concentrations, were plotted as shown in Figure 10. All cases showed diagonal preferential flow of CO_2 from the injector to the producer wells. In Case C-01, the vertical displacement front did not reach the top layers of the reservoir, leaving a large portion of methane unswept. This was attributed to the early CO_2 breakthrough and early well shut-in. Cases C-01, C-02, and C-03 showed water-phase accumulation at the bottom of the reservoir prior to production-well shut-in. In contrast to the other cases, Case C-04 showed a displacement front that swept a significantly larger portion of the reservoir both laterally and vertically. Quantitatively, Case C-02, with the injector well perforated throughout the reservoir thickness and the producer well perforated at the top, was found to be the best option when water is included in the injection process.

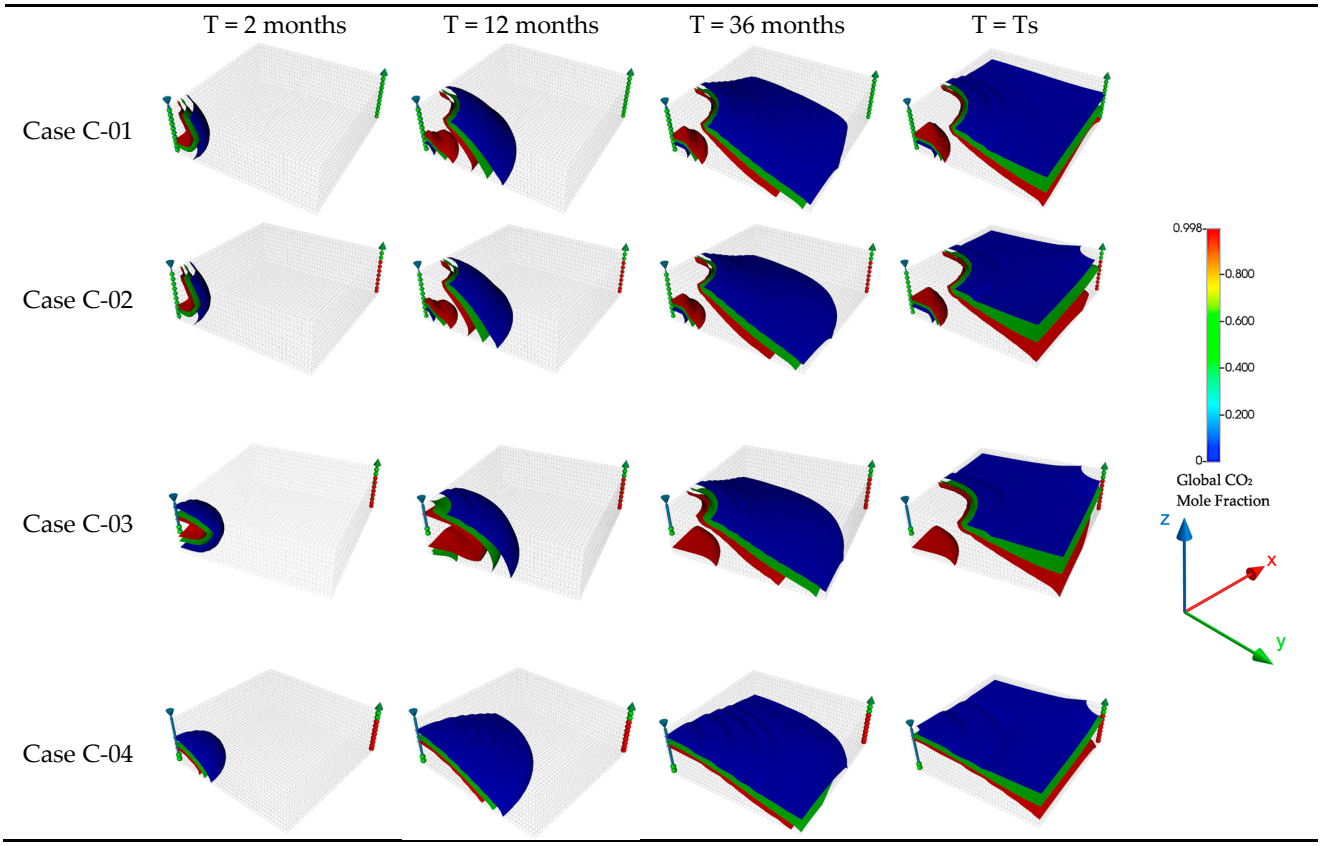

Figure 10. Evolution of global CO_2 mole fraction iso-surfaces showing the effect of producer and injector well perforation depth on CO_2 plume migration and sweep efficiency in a homogeneous reservoir.

4.2.2. Influence of Perforation Depth in Heterogeneous Reservoir

A total of 13 cases from C-05 to C-17 were simulated to analyse the influence of perforation depth in a heterogeneous reservoir. The simulation examined the effects of perforating all layers, varying injector/producer perforation depths, and perforating in higher or lower permeability zones. In all cases, the Case-B1 layered model was used, with the injection stream being the 0.1 water fraction simultaneous injection stream. The injection rate and production pressure at the producer well were the same for all cases. The results are presented in Figure 11 and Table 4.

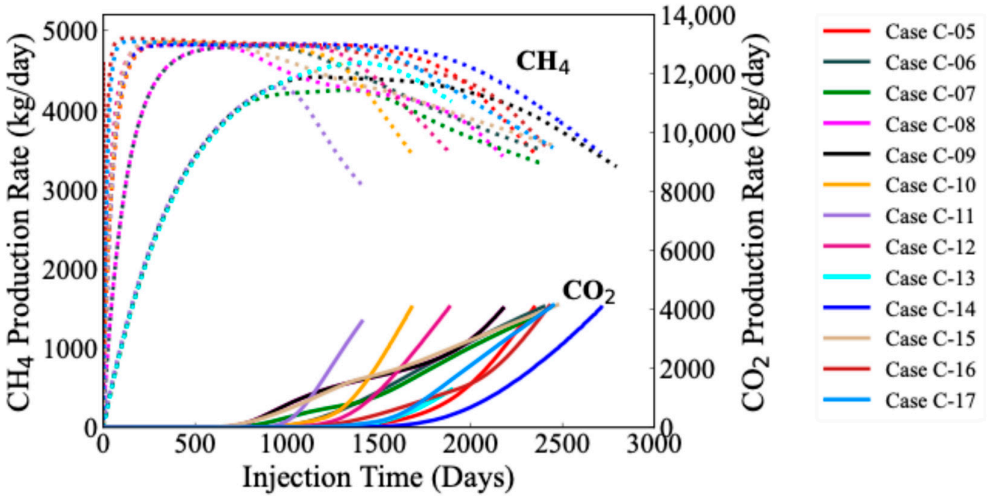

Figure 11. CO_2 and CH_4 mass flow rate for different perforation cases in a heterogeneous reservoir.

Table 4. Injector/producer well perforation depth cases and the simulation results.

Case	Injector Well Perforated Layer	Producer Well Perforated Layer	CO_2 Breakthrough Time (Days)	Producer Well Shut-in Time (Days)	Enhanced CH_4 Recovery (%)	Total CO_2 Sequestrated ($\times 10^4$ Tones)	Solubility Trapped CO_2 (%)	Hysteresis Trapped CO_2 (%)
C-05	10	8	858	2390	21.53	3.852	4.74	11.81
C-06	10	5	1070	2397	25.56	3.854	4.82	11.31
C-07	10	1	1507	2345	21.79	3.924	4.80	11.03
C-08	6	8	1115	2794	26.60	4.571	4.67	11.43
C-09	6	5	770	2176	23.02	3.494	4.77	11.10
C-10	6	1	1066	1677	19.27	2.805	4.75	10.78
C-11	1	4	963	1408	11.59	2.358	4.68	11.82
C-12	1	6	1198	1883	21.68	3.132	4.79	11.21
C-13	1	8	1471	1895	17.86	3.254	4.67	11.63
C-14	1	10	1703	2711	31.26	4.511	4.79	11.16
C-15	All layers	10	758	2472	27.07	3.888	4.74	10.53
C-16	1, 2, 3, 6, 10	4, 5, 7, 8, 9	1279	2518	28.47	4.023	4.47	9.65
C-17	4, 5, 7, 8, 9	1, 2, 3, 6, 10	1419	2538	28.28	4.026	4.79	11.06

The gas mass rates of methane and carbon dioxide for the producer/injector well cases presented in Figure 11 show distinct methane production profiles and carbon dioxide breakthrough curves across the simulated cases. From Table 4, the simulation results indicate that in the heterogeneous reservoir, when the injection well is perforated at the top (cases C-05, 06, and 07), the total CO_2 sequestered and CO_2 breakthrough time increase with producer well perforation depth; hysteresis-trapped CO_2 decreases with depth, while CH_4 enhanced recovery and shut-in time are higher when the producer well is perforated in layers of intermediate depth. When the injector well is perforated in the intermediate layer (cases C-08, 09, and 10), the total sequestered CO_2, the enhanced CH_4 recovery, hysteresis-trapped CO_2, and shut-in time all decrease with increasing producer well perforation depth, whereas the breakthrough time is higher when the producer well is perforated in the top layer. When the injector well is perforated in the lower stratum (cases C-11, 12, 13, and 14), the total CO_2 sequestered, the breakthrough time, and the shut-in time decrease with the producer well perforation depth. In the simulated cases, injection into the lower stratum while simultaneously producing CH_4 from the upper stratum (Case C-14) yields the largest improved recovery of 31.26%. Injection in the higher-permeability zone while producing from the lower-permeability zone (Case C-16) improved recovery

by 28.47%, while the opposite (Case C-17) gave 28.28%. Perforating the injector well in all layers while producing from the upper layer (Case C-15), which was the best option in a homogeneous reservoir, improved recovery by 27.07% in the layered reservoir.

To analyse the influence of water, the results were compared with previous CO_2-EGR studies that did not involve water injection but varied well depth. The findings of this work on injector/producer well perforation depth for higher CH_4 recovery are in agreement with Fan et al.'s [14] findings (injecting at the bottom layer while producing from the top layer) but differ on the producer/injector well perforation for higher CO_2 storage. In their study, only the injection well depth was varied in a subcritical-condition reservoir (3.55 MPa and 66.7 °C) with zero connate water saturation. Patel et al. [21] find that higher recovery, delayed breakthrough time, and higher sequestered CO_2 can be obtained when the injector well is located at the intermediate layers while the producer well is perforated at the top in the presence of connate water saturations. This observation is consistent with the findings of this study on delayed breakthrough time. According to Patel et al. [21], the best performance in CO_2-EGR is obtained when injection is in the intermediate layers and production in the upper layer, and this observation was insensitive to layer heterogeneity. Patel et al.'s [21] suggestion was analysed and compared with the observations in this study, as presented in Figure 12. The results indicate that when water is incorporated in the injection stream and injected in the middle layer, it results in early breakthrough of carbon dioxide, lower recovery (30.05%), and less CO_2 storage (4.466×10^4 tonnes) compared to when the injection is done at the bottom layer and CH_4 is produced at the top layer. Compared to the results of this study, when injection is in the intermediate layers, CO_2 migration was observed to flow through the top layers towards the production well, and the migration was higher through layers with higher permeability, while bottom injection, as suggested by this study, shows a perfect vertical displacement towards the production well.

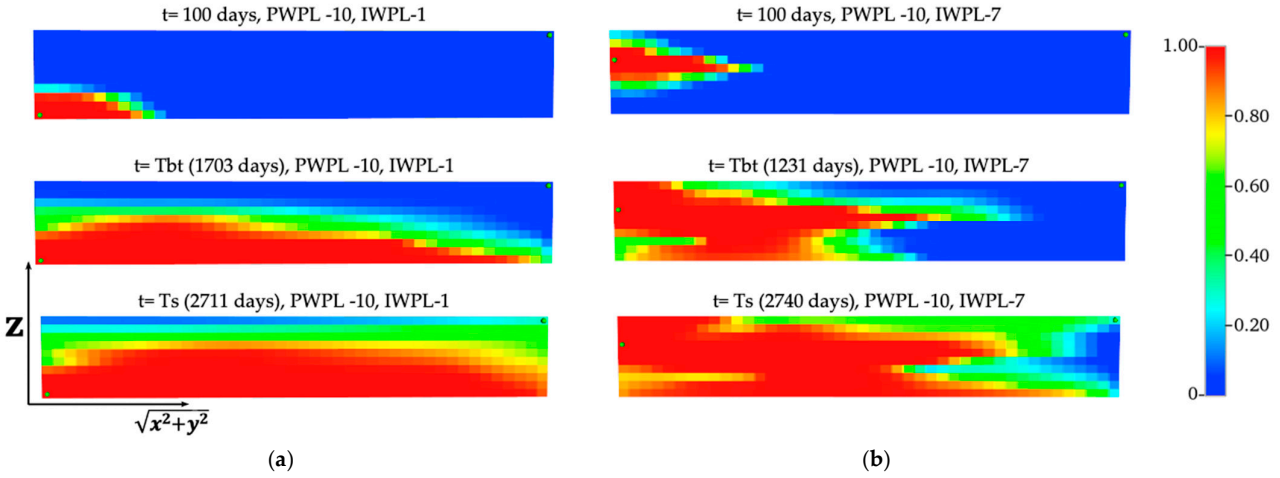

Figure 12. (**a**) CO_2 migration for perforation suggested by this study. (**b**) CO_2 migration for perforations suggested by Patel et al. (PWPL denotes producer well perforated layer, IWPL denotes injector well perforated layer, Ts denotes shut-in time, and Tbt denotes breakthrough time).

4.3. Effect of Injection Rate on EGR and CCS

After determining the perforation depths for the producer and injector wells, the injection rate was analysed in a homogeneous reservoir. Figure 13 shows the mass rate of CH_4 and CO_2 at different injection rates. It can be seen that at a higher injection rate, CH_4 is produced at a higher rate but for a shorter period, while CO_2 breaks through earlier. Table 5 summarises the total injected water pore volume, enhanced recovery, and CO_2

storage efficiency (the amount of CO_2 stored in the reservoir relative to the total CO_2 injected at the time of well shut-in). It can be seen that above the injection rate of 7.5% PV/year, storage efficiency increases with injection rate, while recovery shows the opposite trend. The decrease in CH_4 recovery factor may be attributed to gas entrapment when more water is injected into the reservoir. The results indicate that for higher gas recovery, injection rate and injected water pore volume should not exceed a certain range.

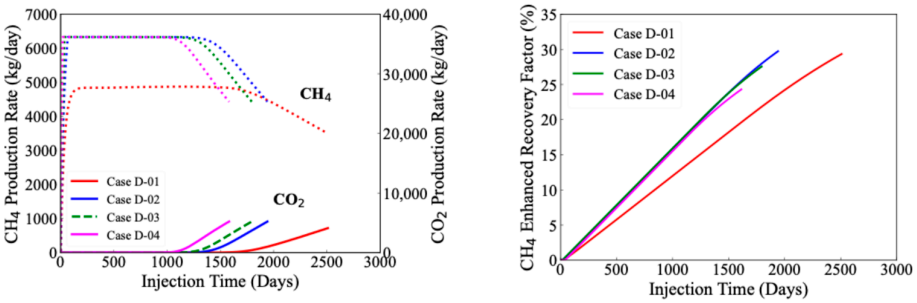

(**a**) (**b**)

Figure 13. Effect of injection rate on (**a**) CO_2 and CH_4 production rate. (**b**) CH_4 enhanced recovery.

Table 5. Comparison of recovery factor and CO_2 storage efficiency for different injection rates.

Case	Injection Rate (%PV/Year)	Cumulative Injected Water PV (-)	CH_4 Enhanced Factor (%)	CO_2 Storage Efficiency (%)
D-01	5.0	0.034	29.35	96.01
D-02	7.5	0.040	29.74	96.93
D-03	10	0.049	27.56	97.62
D-04	15	0.065	24.31	98.31

4.4. Effect of WAG-CO_2 Injection on EGR and CCS

Water and CO_2 alternating injection aimed at analysing CO_2 mobility by alternating water and CO_2 injection rather than simultaneous injection. For consistent comparison, the total water PV injected was held constant, whereas the injected CO_2 PV depended on operational conditions, such as the maximum CO_2 fraction in the production stream. The number of cases ranged from E-01 to E-05, representing continuous injection, single-cycle, and two-, three-, and four-cycle cases, in which water is injected first, followed by CO_2. The final results for CH_4 recovery, total CO_2 storage, and the trapping mechanism, as presented in Figure 14, did not show a significant difference between cyclic and continuous injection. When CO_2 and water were injected simultaneously (Case E-01), gas recovery increased by 29.34%, whereas when WAG-CO_2 was implemented, the best scenario (Case E-02) improved methane recovery by 29.39%. The differences are observed in the early stages of injection, but as the shut-in time approaches, all cases are observed to have equal overall efficiency. This observation can be explained by the effect of water gravity, which is that when the water injection cycle stops, water slumps downward due to gravity, resulting in reopening of the passages that were initially blocked, especially in the top layers, as presented in Figure 15. This phenomenon allows the injected CO_2 during the CO_2 injection cycle to flow through, and the opening occurs sequentially from the top layer down to the bottom layer, also showing the decrease in the amount of water with time after the stoppage of injection, which is due to the evaporation effect.

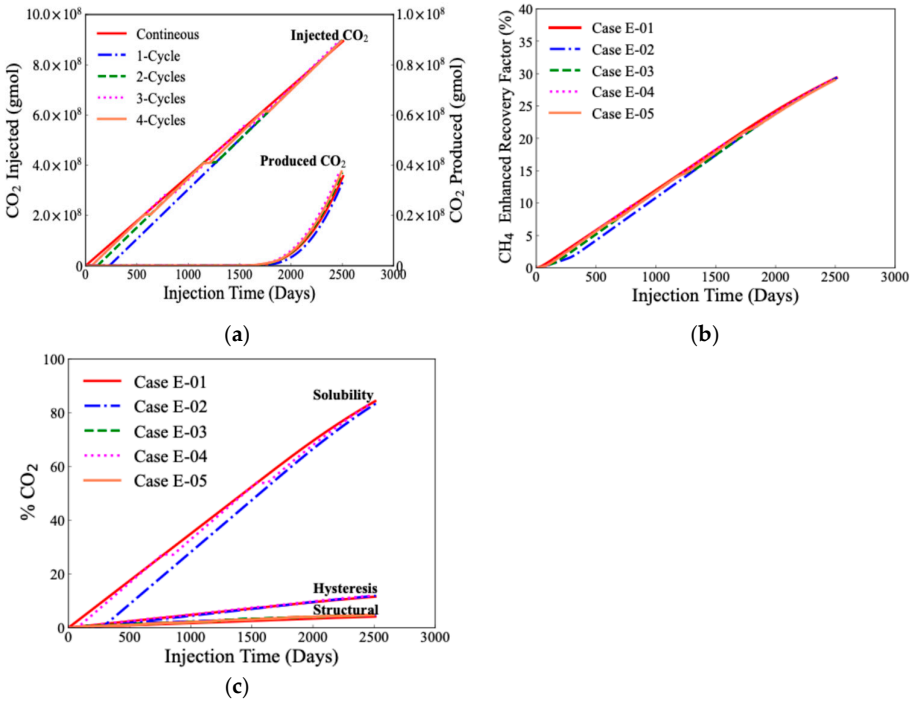

Figure 14. (**a**) Effect of WAG-CO_2 on cumulative CO_2 injected. (**b**) Effect of WAG-CO_2 on CH_4 enhanced recovery. (**c**) Effect of WAG-CO_2 on the CO_2 trapping mechanism.

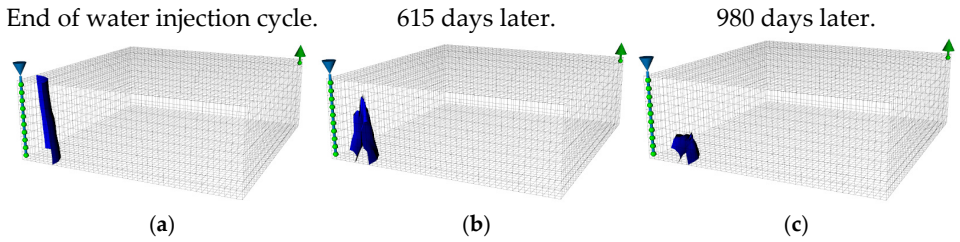

Figure 15. Water saturation iso-surface (S_w = 0.7) indicating water dynamics after stoppage of water injection cycle in homogeneous reservoir.

4.5. CO_2 Storage Behaviour During the EGR Phase

The net stored CO_2, estimated as the difference between total injected and total produced CO_2, was used to estimate storage capacity during the EGR simulation phase for Cases A and B only. The mineral trapping mechanism was not activated in this simulation, leaving residual/hysteresis, solubility, and structure as the trapping mechanisms. The contribution of each trapping mechanism was calculated as the percentage of the total CO_2 trapped that is attributable to each mechanism. The results presented in Figure 16 indicated that the introduction of water reduced the amount of CO_2 stored in the reservoir in Case A, whereas in Case B, the value initially increased to a maximum at a water fraction of 0.05, then decreased as more water was injected. The decrease in CO_2 storage is attributed to water occupying a fraction of the formation pore volume available for storage. However, the presence of injected water changed how CO_2 was stored in the reservoir. Solubility- and hysteresis-trapped carbon dioxide increased with water fraction, while free-phase CO_2 in structural trapping decreased as the water fraction increased. The increase in solubility- and hysteresis-trapped CO_2 reduces buoyant CO_2, thereby lowering leakage risk and improving storage security. The initial increase in CO_2 storage in heterogeneous reservoirs and the improved solubility and hysteresis of trapped CO_2 are consid-

ered positive outcomes for CO_2-EGR, since most real-field reservoirs are heterogeneous in nature.

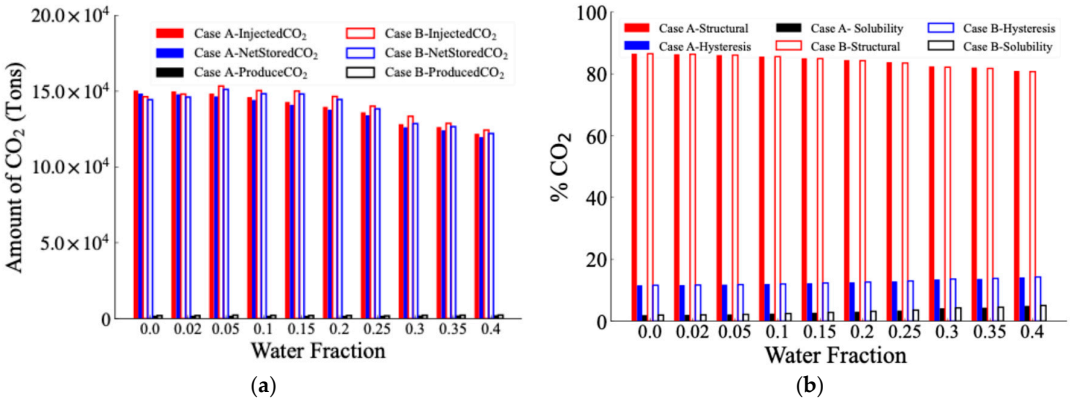

Figure 16. CO_2 inventory during the EGR phase. (**a**) Injected, produced, and trapped CO_2; (**b**) contribution of each trapping mechanism.

4.6. Post-EGR CO_2 Storage and Monitoring

The amount of stored CO_2 and the contribution of each trapping mechanism for Cases A and B are summarised in Table 6. The total injected CO_2 decreased with increasing water fraction. Structural trapping is the dominant trapping mechanism, followed by residual and then solubility trapping. Solubility trapping contributes minimally in the post-EGR simulation because the amount of CO_2 soluble in water is assumed constant at a specific pressure and temperature. At the end of the 100th year of simulation, an increase in soluble and residual trapped CO_2 was observed in some cases. The increase in hysteresis-trapped CO_2 can be explained by the concept of re-imbibition behaviour. When the injection stops, CO_2 migration slows down as the pressure gradient decreases, allowing the displaced fluid to re-enter the pores. At this moment, the gas relative permeability follows the imbibition curve, leading to the entrapment of disconnected CO_2

Table 6. Total CO_2 inventory for the overall injection programme.

	Water Fraction	Amount of CO_2 Trapped (Mill. Tons)	Contribution of Each Trapping Mechanism at the End of Injection (%)			Contribution of Each Trapping Mechanism at the End of Simulation Time (100 Years) (%)		
			Structural	Residual	Solubility	Structural	Residual	Solubility
Case A	0.00	0.1485	86.53	11.57	1.90	86.50	11.57	1.93
	0.02	0.1480	86.36	11.65	1.99	86.33	11.65	2.02
	0.05	0.1466	86.09	11.77	2.14	86.05	11.78	2.17
	0.10	0.1442	85.62	11.99	2.40	85.57	12.00	2.43
	0.15	0.1410	85.07	12.24	2.69	85.04	12.24	2.73
	0.20	0.1378	84.47	12.51	3.02	84.45	12.50	3.05
	0.25	0.1342	83.79	12.83	3.38	83.81	12.79	3.40
	0.30	0.1262	82.74	13.25	4.00	82.43	13.46	4.12
	0.35	0.1242	82.41	13.40	4.19	82.06	13.62	4.32
	0.40	0.1197	81.42	13.84	4.73	80.97	14.12	4.91
Case B1	0.00	0.1444	86.52	11.57	1.91	86.48	11.57	1.96
	0.02	0.1461	86.36	11.64	2.00	86.31	11.64	2.04
	0.05	0.1512	86.08	11.78	2.14	86.03	11.78	2.18
	0.10	0.1483	85.58	12.00	2.42	85.53	12.00	2.47
	0.15	0.1482	84.94	12.30	2.76	84.91	12.29	2.80

0.20	0.1446	84.27	12.61	3.12	84.26	12.59	3.15
0.25	0.1384	83.68	12.84	3.48	83.5	12.97	3.53
0.30	0.1286	82.54	13.34	4.12	82.16	13.59	4.25
0.35	0.1266	82.19	13.50	4.31	81.77	13.77	4.46
0.40	0.1221	81.29	13.90	4.81	80.73	14.25	5.02

5. Conclusions

This study used numerical simulation to investigate the inclusion of water injection in the CO_2-EGR process. The investigation examined the influence of water on both enhanced gas recovery and CO_2 storage in both heterogeneous and homogeneous reservoirs, compared continuous and cyclic injection strategies, and evaluated the effect of perforation depth and injection rate. The overall outcomes are summarised below:

- Inclusion of water in CO_2 injection for both EGR and CS improves natural gas recovery in both homogeneous and heterogeneous reservoirs. The inclusion of water injection resulted in an additional increase of up to 1.55% gas recovery in the homogeneous reservoir and up to 8.04% in the heterogeneous reservoir compared to when only CO_2 is used. It was concluded that the improved gas recovery factor and the CO_2 storage are affected by both formation properties and operation factors such as heterogeneity, injection strategy, and the injector and producer well perforation depth.
- Perforation depth affects gas recovery and CO_2 storage. When the producer well is perforated at the top stratum of the reservoir, and the injector well is fully perforated throughout, the reservoir depth gives a higher recovery than other options.
- Higher injection rates result in higher injected water and higher storage of CO_2 at the time of well shut-in, but it gives a lower recovery factor, which could be attributed to gas entrapment from injected water. Therefore, for higher EGR, a lower injection rate is the better option.
- The findings in this study indicate that different CH_4 enhanced recovery and CO_2 storage values are obtained in water–CO_2 EGR depending on water content, injection rate and injection depth. Therefore, co-optimisation of injection rate and amount of water for any given reservoir depth constrained to higher gas recovery and CO_2 storage should be done to provide a practical guide.
- This study limited its scope on closed boundary reservoir and assumed a reservoir without aquifer influx. However, most mature gas reservoirs experience aquifer influx and higher water production. Therefore, a study on the performance of water–CO_2 EGR needs to be done to improve the practical application.

Author Contributions: Conceptualization, A.N.R. and Y.S.; methodology, A.N.R. and Y.S.; software, A.N.R. and Y.S.; validation, A.N.R., Y.S., T.E., and T.T.; formal analysis, A.N.R.; investigation, A.N.R.; resources, Y.S.; data curation, A.N.R.; writing—original draft preparation, A.N.R.; writing—review and editing, A.N.R., T.E., and T.T.; visualisation, A.N.R.; supervision, Y.S.; project administration, Y.S.; funding acquisition, Y.S. All authors have read and agreed to the published version of the manuscript.

Funding: This research received no external funding.

Data Availability Statement: All data, codes, and information used in this study are available upon request from the authors.

Acknowledgments: The authors thank Computer Modelling Group Ltd. for supporting an academic software licence for Kyushu University.

Conflicts of Interest: The authors declare no conflicts of interest.

Nomenclature

Abbreviations	
CCUS	Carbon capture utilisation and storage
EGR	Enhanced gas recovery
IWPL	Injector well perforated layer
PV	Pore volume
PWPL	Production well perforated layer
PR-EOS	Peng–Robinson equation of state
RF	Recovery factor
WAG	Water alternating gas
List of symbols	
H_{CO_2}	CO_2 Henry's constant (MPa)
k_r	Gas relative permeability (-)
D	Diffusion coefficient (cm^2/s)
f	Fugacity (MPa)
g	Gravity acceleration (m^2/s)
k	Permeability (mD)
P	Pressure (MPa)
P_d	Threshold capillary pressure (MPa)
q	Mass flow rate per unit volume ($kg/m^3/s$)
S	Water saturation
T	Temperature (K)
V	Volume (m^3)
X	Mass fraction
x	Mole fraction
Greek Letters	
ϕ	Porosity
β	Phase
κ	Mixture component
τ	Tortuosity
λ	Pore size distribution
ρ	Density (kg/m^3)

References

1. International Energy Agency. *The Role of Gas in Today's Energy Transitions*; International Energy Agency: Paris, France, 2019.
2. Gürsan, C.; de Gooyert, V. The Systemic Impact of a Transition Fuel: Does Natural Gas Help or Hinder the Energy Transition? *Renew. Sustain. Energy Rev.* **2021**, *138*, 110552.
3. Dupont, C.; Oberthür, S. Insufficient Climate Policy Integration in EU Energy Policy: The Importance of the Long-Term Perspective. *J. Contemp. Eur. Res.* **2012**, *8*, 228–247.
4. Hanson, E.; Nwakile, C.; Hammed, V.O. Carbon Capture, Utilization, and Storage (CCUS) Technologies: Evaluating the Effectiveness of Advanced CCUS Solutions for Reducing CO_2 Emissions. *Results Surf. Interfaces* **2025**, *18*, 100381. https://doi.org/10.1016/j.rsurfi.2024.100381.
5. Blok, K.; Williams, R.H.; Katofsky, R.E.; Hendriks, C.A. Hydrogen Production from Natural Gas, Sequestration of Recovered CO_2 in Depleted Gas Wells and Enhanced Natural Gas Recovery. *Energy* **1997**, *22*, 161–168.
6. Pales, A.F.; Bennett, S. *Energy Technology Perspectives 2020*; International Energy Agency: Paris, France, 2020; 400p.
7. Bui, M.; Adjiman, C.S.; Bardow, A.; Anthony, E.J.; Boston, A.; Brown, S.; Fennell, P.S.; Fuss, S.; Galindo, A.; Hackett, L.A.; et al. Carbon Capture and Storage (CCS): The Way Forward. *Energy Environ. Sci.* **2018**, *11*, 1062–1176.
8. Raihan, A. Carbon Capture, Utilization, and Storage (CCUS) in the Context of Earth Energy Systems: A Multidisciplinary Review. *Geosci. Front.* **2025**, *16*, 102177. https://doi.org/10.1016/j.gsf.2025.102177.
9. Haq, B.; Salahu Muhammed, N.; Liu, J.; Tong Chua, H. Enhanced Natural Gas Production Using CO_2 Injection: Application to Sustainable Hydrogen Production. *Fuel* **2023**, *347*, 128474.
10. Van Der Burgt, M.J.; Cantle, J.; Boutkan, V.K. Carbon Dioxide Disposal from Coal Based IGCC's in Depleted Gas Field. *Energy Convers. Manag.* **1992**, *33*, 603–610.

11. Oldenburg, C.M.; Stevens, S.H.; Benson, S.M. Economic Feasibility of Carbon Sequestration with Enhanced Gas Recovery (CSEGR). *Energy* **2004**, *29*, 1413–1422. https://doi.org/10.1016/j.energy.2004.03.075.
12. Oldenburg, C.M.; Pruess, K.; Benson, S.M. Process Modeling of CO_2 Injection into Natural Gas Reservoirs for Carbon Sequestration and Enhanced Gas Recovery. *Energy Fuels* **2001**, *15*, 293–298. https://doi.org/10.1021/ef000247h.
13. Hughes, T.J.; Honari, A.; Graham, B.F.; Chauhan, A.S.; Johns, M.L.; May, E.F. CO_2 Sequestration for Enhanced Gas Recovery: New Measurements of Supercritical CO_2-CH_4 Dispersion in Porous Media and a Review of Recent Research. *Int. J. Greenh. Gas Control* **2012**, *9*, 457–468. https://doi.org/10.1016/j.ijggc.2012.05.011.
14. Amin, R.; Sidiq, H.; Kennaird, T.; Van der Steen, E. Gas-Gas Experimental Interfacial Tension Measurement. *Fluid Phase Equilib.* **2010**, *295*, 230–236. https://doi.org/10.1016/j.fluid.2010.05.020.
15. Fan, L.; Tan, Q.; Li, H.; Xu, J.; Wang, X.; Liu, S. Simulation on Effects of Injection Parameters on CO_2 Enhanced Gas Recovery in a Heterogeneous Natural Gas Reservoir. *Adv. Theory Simul.* **2021**, *4*, 2100127. https://doi.org/10.1002/adts.202100127.
16. Rebscher, D.; May, F.; Oldenburg, C.M. Sequestration of CO_2 in the Altmark Natural Gas Field, Germany: Mobility Control to Extend Enhanced Gas Recovery. In Proceedings of the TOUGH Symposium, Berkeley, CA, USA, 15–17 May 2006.
17. Abba, M.K.; Al-Othaibi, A.; Abbas, A.J.; Nasr, G.G.; Mukhtar, A. Experimental Investigation on the Impact of Connate Water Salinity on Dispersion Coefficient in Consolidated Rocks Cores during Enhanced Gas Recovery by CO_2 Injection. *J. Nat. Gas Sci. Eng.* **2018**, *60*, 190–201. https://doi.org/10.1016/j.jngse.2018.10.007.
18. Clemens, T.; Secklehner, S.; Mantatzis, K.; Jacobs, B. Enhanced Gas Recovery, Challenges Shown at the Example of Three Gas Fields. In *Proceedings of the SPE EUROPEC/EAGE Annual Conference and Exhibition, Barcelona, Spain, 14–17 June 2010*; SPE: Richardson, TX, USA, 2010; p. 130151.
19. Liu, S.; Zhang, Y.; Xing, W.; Jian, W.; Liu, Z.; Li, T.; Song, Y. Laboratory Experiment of CO_2-CH_4 Displacement and Dispersion in Sandpacks in Enhanced Gas Recovery. *J. Nat. Gas Sci. Eng.* **2014**, *26*, 1585–1594. https://doi.org/10.1016/j.jngse.2015.04.021.
20. Zhao, E.M.; Jin, Z.J.; Li, G.S.; Zhang, K.Q.; Zeng, Y. Feasibility of CO_2 Storage and Enhanced Gas Recovery in Depleted Tight Sandstone Gas Reservoirs within Multi-Stage Fracturing Horizontal Wells. *Pet. Sci.* **2024**, *21*, 4189–4203. https://doi.org/10.1016/j.petsci.2024.08.014.
21. Patel, M.J.; May, E.F.; Johns, M.L. High-Fidelity Reservoir Simulations of Enhanced Gas Recovery with Supercritical CO_2. *Energy* **2016**, *111*, 548–559. https://doi.org/10.1016/j.energy.2016.04.120.
22. Sim, S.S.K.; Turta, A.T.; Singhal, A.K.; Hawkins, B.F. Enhanced Gas Recovery: Factors Affecting Gas-Gas Displacement Efficiency. *J. Can. Pet. Technol.* **2009**, *48*, 49–55.
23. Patel, M.J.; May, E.F.; Johns, M.L. Inclusion of Connate Water in Enhanced Gas Recovery Reservoir Simulations. *Energy* **2017**, *141*, 757–769. https://doi.org/10.1016/j.energy.2017.09.074.
24. He, C.; Ji, Z.; Geng, X.; Zhou, M. The Influence of Irreducible Water for Enhancing CH_4 Recovery in Combination of CO_2 Storage with CO_2 Injection in Gas Reservoirs. *Int. J. Greenh. Gas Control* **2023**, *126*, 103919. https://doi.org/10.1016/j.ijggc.2023.103919.
25. Zecca, M.; Vogt, S.J.; Honari, A.; Xiao, G.; Fridjonsson, E.O.; May, E.F.; Johns, M.L. Quantitative Dependence of CH_4-CO_2 Dispersion on Immobile Water Fraction. *AIChE J.* **2017**, *63*, 5159–5168. https://doi.org/10.1002/aic.15824.
26. Omar, A.; Addassi, M.; Vahrenkamp, V.; Hoteit, H. Co-Optimization of CO_2 Storage and Enhanced Gas Recovery Using Carbonated Water and Supercritical CO_2. *Energies* **2021**, *14*, 7495. https://doi.org/10.3390/en14227495.
27. Cason, L.D., Jr. Waterflooding Increases Gas Recovery. *J. Pet. Technol.* **1989**, *41*, 1102–1106.
28. Fishlock, T.P.; Probert, C.J.; Technology, A. Waterflooding of Gass Condensate Reservoirs. *SPE Res. Eng.* **1996**, *11*, 245–*251.*
29. Matthews, J.D.; Hawes, R.I.; Hawkyard, I.R.; Fishlock, T.P. Feasibility Studies of Waterflooding Gas-Condensate Reservoirs. *J. Pet. Technol.* **1988**, *40*, 1049–1056.
30. Khoshnevis, N.; Khosrokhavar, R.; Nick, H.M.; Bruhn, D.F.; Bruining, H. Injection of Disposal Water from a Geothermal Reservoir into a Gas Reservoir. *J. Pet. Sci. Eng.* **2019**, *178*, 616–628. https://doi.org/10.1016/j.petrol.2019.03.016.
31. Walker, T. Enhanced Gas Recovery Using Pressure and Displacement Management Management. Master's Thesis, Louisiana State University, Baton Rouge, LA, USA, 2002.
32. Valjak, M.; Novakovic, D.; Bassiouni, Z. Physical and Economic Feasibility of Waterflooding of Low-Pressure Gas Reservoirs. In Proceedings of the SPE Latin American and Caribbean Petroleum Engineering Conference, Buenos Aires, Argentina, 25–28 March 2001.
33. Biagi, J.; Agarwal, R.; Zhang, Z. Simulation and Optimization of Enhanced Gas Recovery Utilizing CO_2. *Energy* **2016**, *94*, 78–86. https://doi.org/10.1016/j.energy.2015.10.115.
34. Abdoulghafour, H.; Sarmadivaleh, M.; Hauge, L.P.; Fernø, M.; Iglauer, S. Capillary Pressure Characteristics of CO_2-Brine-Sandstone Systems. *Int. J. Greenh. Gas Control* **2020**, *94*, 102876. https://doi.org/10.1016/j.ijggc.2019.102876.

35. Ni, H.; Li, B.; Darraj, N.; Ren, B.; Harris, C.; Krishnamurthy, P.G.; Bukar, I.; Berg, S.; Snippe, J.; Ringrose, P.; et al. The Impact of Capillary Heterogeneity on CO_2 Flow and Trapping across Scales. *Earth. Sci. Rev.* **2025**, *270*, 105257.
36. Class, H.; Ebigbo, A.; Helmig, R.; Dahle, H.K.; Nordbotten, J.M.; Celia, M.A.; Audigane, P.; Darcis, M.; Ennis-King, J.; Fan, Y.; et al. A Benchmark Study on Problems Related to CO_2 Storage in Geologic Formations: Summary and Discussion of the Results. *Comput. Geosci.* **2009**, *13*, 409–434. https://doi.org/10.1007/s10596-009-9146-x.
37. Liu, S.; Agarwal, R.; Sun, B. Numerical Simulation and Optimization of CO_2-Enhanced Gas Recovery in Homogeneous and Vertical Heterogeneous Reservoir Models. *J. Energy Resour. Technol. Trans. ASME* **2022**, *144*, 033009. https://doi.org/10.1115/1.4053299.